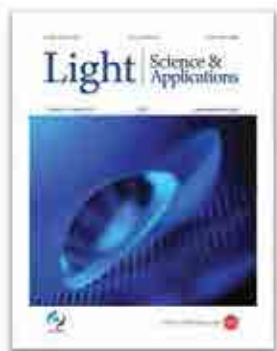**Accepted Article Preview: Published ahead of advance online publication**

Quantifying single plasmonic nanostructure far-fields with interferometric and polarimetric k-space microscopy

Ruslan Rörich, Chris Hoekmeijer, Clara I. Osorio and A. Femius Koenderink

This is a PDF file of an unedited peer-reviewed manuscript that has been accepted for publication. NPG are providing this early version of the manuscript as a service to our customers. The manuscript will undergo copyediting, typesetting and a proof review before it is published in its final form. Please note that during the production process errors may be discovered which could affect the content, and all legal disclaimers apply.

1   succinct title:

2   **Quantifying single plasmonic nanostructure far-fields with interferometric and**
3   **polarimetric k-space microscopy**

4

5   concise running title:

6   **Quantitative single nanostructure far-fields**

7

8   **Ruslan Röhrich**

9   Center for Nanophotonics, AMOLF, Science Park 104, 1098 XG Amsterdam, The
10 Netherlands

11 ARCNL, Science Park 110, 1098 XG Amsterdam

12 Email: r.rohrich@amolf.nl

13 **Chris Hoekmeijer**

14 Center for Nanophotonics, AMOLF, Science Park 104, 1098 XG Amsterdam, The
15 Netherlands

16 Email: chris_hoekmeijer@hotmail.com

17 **Clara I. Osorio**

18 Center for Nanophotonics, AMOLF, Science Park 104, 1098 XG Amsterdam, The
19 Netherlands

20 Email: clara.osoriotamayo@tno.nl

21 **A. Femius Koenderink***

22 Center for Nanophotonics, AMOLF, Science Park 104, 1098 XG Amsterdam, The
23 Netherlands

24 email: f.koenderink@amolf.nl

25 phone: 0031207547189

26

27

Abstract

Optically resonant nanoantennae are key building blocks for metasurfaces, nanosensors and nanophotonic light sources due to their ability to control the amplitude, phase, directivity and polarization of scattered light. Here, we report an experimental technique for the full recovery of all degrees of freedom encoded in the far-field radiated by a single nanostructure using a high-NA Fourier microscope equipped with digital off-axis holography. This method enables full decomposition of antenna-physics in its multipole contributions and gives full access to the orbital and spin angular momentum properties of light scattered by single nano-objects. Our results demonstrate these capabilities through a quantitative assessment of the purity of the 'selection rules' for orbital angular momentum transfer by plasmonic spiral nanostructures.

Introduction

A cornerstone of nanophotonics is to precisely control the resonances of individual metallic and dielectric scatterers that form elementary building blocks of nanophotonic devices such as metasurfaces and nanoantennae. The underlying physics is based on the fact that subwavelength geometric tailoring controls the near-field multipolar resonances of nanoscatterers, which in turn allows for a precise manipulation of the amplitude, phase and polarization of light scattered into the far field. For instance, the past decade has seen the realization of plasmonic nanoantennae[1-3] to tailor directivity[4-8] and polarization[9-12] of scattering and fluorescence, even down to the level of single-photon sources[13]. Additionally, metasurfaces based on metallic and dielectric nanoresonators provide near-arbitrary control over the phase, amplitude, spin and orbital angular momentum content of transmitted wavefronts[14-17].

Even though a successful design requires a precise understanding of the type of multipolar resonances supported by a nano-object, the complex superposition one can excite, and how these radiate into the far field, such an understanding commonly relies largely on numerical results and is supported only indirectly by experimental evidence. In principle, a measurement of the *full* polarization, amplitude and phase of light for each angle in the 4π far-field radiation pattern of a nanoantenna enables full decomposition of the antenna's response in its locally induced multipoles (see Fig. 1). Thus, full field radiation pattern measurement at all angles can enable complete nanoantenna polarizability tomography. In this work, we present a phase- and polarization-resolved Fourier microscope that meets this challenge over the NA spanned by a high-NA microscope objective. We demonstrate the potential of this method by phase resolving the radiation pattern of single spiral-shaped nanoscatterers that generate orbital angular momentum (OAM)[18]. OAM beams have envisioned applications in optical communication technology[19,20], quantum information processing[21] and optical manipulation[22]. Since these applications require a precise knowledge of the OAM mode

66 content, the detection and analysis of paraxial OAM beams has been a subject of great
67 interest[23-26]. However, a quantitative assessment of the purity with which plasmonic
68 nanostructures, such as spiral nanostructures, transfer OAM to scattered, spherical
69 waves is still missing. Here, we present such measurement results, which not only
70 demonstrate the capabilities of our technique but are also highly relevant in view of
71 shrinking applications for OAM beams to length scales of, e.g., single-photon emitters.

72 In addition to opening up new possibilities in the research of nanoantennae and
73 metasurfaces, we envision that the proposed method will have a large impact on optical
74 metrology applications[27].

Results

Experimental set-up

77 Our novel experimental technique for angle-resolved amplitude, polarization and phase
78 imaging of single nano-objects is based on a combination of Fourier microscopy,
79 polarimetry and digital holography. As Fig. 2 a) illustrates, the basis is a high-NA
80 imaging microscope composed of a HeNe laser source ($\lambda = 633$ nm), a 100x objective
81 (Nikon, NA $= 0.9$), a 20 cm tube lens and a CCD camera. Additionally, a Fourier lens
82 ($f = 200$ mm) is inserted such that its focal point (after being relayed by a 4f-telescope)
83 lies in the back focal plane of the microscope objective, with the Fourier plane of the
84 sample projected onto the CCD camera. This projection maps the in-plane wavevectors
85 $\mathbf{k}_\parallel$ of the scattered light with a high angular precision of approximately 0.5° over the full
86 70° opening angle of the objective[28,29]. Two Stokes polarimeters enable one to control
87 and measure the full polarization state of incoming and outgoing light for each wave
88 vector[30], on the proviso that one accounts for the conversion of the spherical waves
89 scattered from the nanostructures to paraxial cylindrical beams by the microscope
90 objective. Next, this setup utilizes off-axis digital holography for phase resolution[31-32] by
91 mixing the object beam, which contains the wave front scattered by a single
92 nanostructure, with a reference beam derived from the same laser. This technique has
93 the advantage of operating in a single-shot manner by making use of single digitally
94 Fourier-transformed camera images for phase resolution, as opposed to delay scanning.
95 Although digital holographic microscopy was recently applied to nanophotonic
96 structures[33-36], these studies were mostly aimed at real space, i.e., sample plane,
97 imaging. However, real-space images of nanoantennae have the drawback of being
98 restricted by the diffraction limit and, therefore, typically cover just a few camera pixels.
99 In contrast, Fourier-space holography of single nanoantennae generates a signal over
100 an entire CCD chip, providing far richer information.

Spiral nanostructures

102 We demonstrate the large potential of Fourier-space holography by applying it to single
103 plasmonic bullseye and spiral nanostructures, which are expected to generate significant
104 orbital angular momentum content and spin-orbit coupling signatures in their
105 response[11,30,37,38]. The nanostructures consist of grooves milled with a focused ion beam
106 around a central aperture, where the groove duty cycle is 50 %, and the groove-groove
107 spacing (pitch) is 500 nm, selected for operation near the wavelength of 633 nm. The
108 structures are milled in a 200 nm optically thick gold film evaporated onto a glass
109 coverslip; see Fig. 2 b) and c) for a schematic and scanning electron micrograph.
110 Throughout the text the handedness of the spirals is defined when looking along the
111 wave propagation direction. Using this convention, m denotes the number of spiral
112 grooves with $m > 0$ for clockwise (CW), $m < 0$ for counter-clockwise (CCW) spirals and
113 $m = 0$ for bullseye structures. While the single sub-wavelength aperture is a non-
114 directional scatterer, the grooves are expected to generate directional outcoupling
115 ("beaming") of surface plasmon polaritons (SPPs) that are launched when exciting the
116 aperture[4,39]. According to earlier reports, [37,40] these structures should imprint OAM onto
117 scattered light, governed by the propagation delay experienced by the SPPs en route
118 from the aperture to the outcoupling grooves and through a phenomenon called spin-
119 orbit coupling[41-43], which introduces changes between the incident and the outgoing spin
120 angular momentum (SAM). For plane waves, SAM is associated with helicity so that
121 $\sigma = +1$ and $\sigma = -1$ for right-hand circular (RHC) and left-hand circular (LHC)
122 polarizations, respectively. Additionally, in this case, the term OAM does not refer to the
123 common OAM studied for paraxial, cylindrical beams, but rather indicates that the
124 scattered spherical wave $\mathbf{S}(\theta, \phi)\dfrac{e^{ikR}}{R}$ carries helical phase fronts of the form $\exp(il\phi)$ in
125 its complex scattering amplitude function. Here, l is an integer and ϕ is the azimuthal
126 angle, while we denote the angle relative to the optical axis through the gold film by θ.

Experimental workflow

128 Figure 3 highlights the main measurement modalities required to fully quantify an
129 antenna radiation pattern, taking a $m = -5$ spiral nanostructure with RHC excitation
130 (input polarization indicated as green arrows in all figures) as an example. First and
131 foremost, our setup is a Fourier microscope, which enables one to record the intensity
132 radiation pattern $|\mathbf{S}(\theta, \phi))|^2$ or more precisely $|\mathbf{S}(k_x, k_y)|^2 dk_x dk_y$ with $(k_x, k_y) =$
133 $(\cos\phi\sin\theta, \sin\phi\sin\theta)$. The intensity distribution in Fig. 3 a) (logarithmic scale) was
134 measured by removing the polarization filters (QWP$_2$, LP$_2$ and HWP) in the collection
135 path and blocking the reference beam in the setup shown in Fig. 2 a). It features a high
136 intensity peak in its center, which signifies strong beaming into a narrow cone of angles
137 normal to the sample. As shown in previous studies, this is a consequence of diffractive
138 outcoupling of surface plasmon polaritons by the grooves[4,30,39]. This beaming stands in
139 sharp contrast to an isolated hole, which would produce an isotropic pattern[30]. The $|m|$

140 spiraling fringes and oscillations in the radial direction in the intensity map are caused by
141 interference of the near-spherical wave scattered by the central aperture and the
142 helically phase wave out-coupled by the spiral grooves[37].

143 The second capability of the setup, namely, polarization-resolved imaging, relies on
144 measurements of intensity profiles in different output polarization bases (linear along
145 $0°, 45°, 90°, 135°$ and circular left and right, red arrows indicate polarization in each panel)
146 to determine the Stokes parameters. An example raw data set with the corresponding
147 Stokes parameter results is reported in the Supplementary. The Stokes parameters S_i
148 with $i = 0,1,2,3$ fully characterize the polarization state of the wavefront for each
149 collected wave vector in the radiation pattern[44] and can therefore be converted into a
150 polarization ellipse for each detected wave vector in the radiation pattern (see methods
151 section). Fig. 3 b) reports the polarization ellipse parameters, namely, the ellipticity angle
152 ϵ ($\epsilon = 0$ for linear polarization, resp. $\pm \pi /4$ for RHC/LHC polarization) and the
153 orientation α of the major axis of the ellipse relative to the k_x axis. In the particular case
154 of RHC input polarization, $\epsilon = -\pi/4$ represents full helicity conversion, and $\epsilon = \pi/4$
155 represents the retained polarization. The wavevector-resolved ϵ map in Fig. 3 b) clearly
156 shows complete helicity conversion ($\epsilon = -\pi/4$) in a doughnut-like shape with five
157 spiraling arms around it. Regions close to these features are characterized by an equal
158 distribution of LHC and RHC polarization ($\epsilon = 0$, linear polarization), with the remaining
159 k-space containing an unchanged helicity ($\epsilon = \pi/4$). This directly evidences helicity
160 conversion at oblique scattering angles, i.e., spin-orbit coupling in scattering. The reader
161 should note that since the nanostructure scatters the incident beam (cylindrical
162 geometry) into a spherical wave, the polarization definition is not trivial. For instance,
163 given that our input polarization RHC implies an input E-field vector along $(\hat{x} + i\hat{y})/$
164 $\sqrt{2}$ (with z the optical axis), the definition of the helicity conserving/reversing channel
165 actually means projection of the full measured field **S** on $(\hat{\theta} \pm i\hat{\phi})/\sqrt{2}$.

166 Finally, while the Stokes parameter measurements allow for the retrieval of *phase*
167 *differences* between two orthogonally polarized field components, by adding digital
168 holographic microscopy capabilities to the setup, we are able to measure the individual
169 *phase profiles* of the respective polarization states. More specifically, we make use of
170 digital off-axis holography. To this end, the reference beam E_R, polarized identical to the
171 detection channel, is overlapped with the object wave $E_O = |E_O| \exp[-i\varphi]$, i.e., the
172 Fourier-space image, on the CCD camera, which results in the hologram H $= |E_O + E_R|^2$.
173 Considering the simplest case of the reference beam being a plane wave with $E_R =$
174 $|E_R| \exp[-i\vec{k} \cdot \vec{x} \, sin\delta]$, where $\vec{k}$ is its wavevector and δ the angle between the object and
175 reference beam, the hologram H can be mathematically expressed as

176
$$H = |E_O|^2 + |E_R|^2 + |E_O \cdot E_R| \exp[\pm i(\varphi + \vec{k} \cdot \vec{x} \, sin\delta)] \quad (1)$$

177 From this equation, it becomes apparent that only the cross terms contain φ, which is
178 the object wave phase information. The additional phase term $\vec{k} \cdot \vec{x} \sin\delta$ arises from the
179 deliberately introduced tilt δ, which serves to separate the cross and direct terms upon
180 digital Fourier transformation. Figure 3 c) shows such a digital Fourier transform of the
181 hologram corresponding to a $m = -5$ spiral in circular co-polarization. This inclination
182 angle δ is chosen to be sufficiently large such that upon Fourier transformation, the
183 cross and direct terms are well separated yet sufficiently small that the hologram fringes
184 are well sampled by the pixelated detector. The remaining digital reconstruction process
185 consists of selecting (i.e., binary masking), shifting, back-Fourier transforming one of the
186 cross-terms and a digital correction for residual parabolic phase aberrations in the
187 imaging optics (see methods section). Figure 3 d) shows two measured phase maps for
188 the co- and cross-polarized channel. They reveal a helical evolution of the phase around
189 the optical axis, which is especially evident for the cross-polarized channel. The phase
190 profile in the co-polarized channel contains five spiraling arms, with an overall phase
191 increment of $5 \cdot 2\pi$ when going full circle around the origin. The phase profile in the
192 cross-polarized channel contains 2 fewer arms and an additional feature around its
193 center. The origin of these effects will be further discussed in the next section.

Analysis of spiral radiation patterns

195 Having introduced the experimental workflow for full quantification of the amplitude,
196 polarization and phase information in the radiation of a nano-object, we present an
197 example of the type of rich insight one can gain. For plasmonic spirals, we conducted an
198 in-depth quantification of their OAM-conversion efficiency depending on their geometry,
199 i.e., on the number of arms. Figure 4 a) and c) demonstrate a subset of the measured
200 full electric fields radiated into the polarization-helicity-conserving and helicity-changing
201 channel using RHC input polarization. To support our measured results, we show the
202 simulated field profiles of the corresponding spiral/ bullseye structures in Figs. 4 b) and
203 d), which demonstrate a good qualitative agreement. These plots show simultaneously
204 the field phase (from hologram) as hue and the field amplitude ($|\boldsymbol{S}(\theta, \phi)|$) as brightness
205 (logarithmic scale). Figure 4 highlights results for CCW spirals with up to 9 arms
206 ($m = -9$), starting from the case of a bullseye ($m = 0$). It is evident that the number of
207 spiral grooves $|m|$ has a big impact on both the amplitude and phase in both co- and
208 cross-polarized measurements. As in Fig. 3 d), the number of spiraling arms in the
209 Fourier maps coincides with the number of arms of the spirals in co-polarization, while in
210 cross-polarization, the field profiles show 2 fewer arms. These arms are visible both in
211 the amplitude and phase because they bring a phase increment of 2π per arm when
212 traversing a circle at constant θ through the radiation pattern. These observations
213 highlight that OAM conversion is controlled by a combination of propagation phase
214 (number of arms) and SAM conversion (± 2 for helicity-reversing scattering). We refer to
215 Fig. S4 in the Supplementary for further examples with the same input/output

216 polarization settings but with a reversed spiral orientation ($m > 0$). In this case, not only
217 does the orientation of the field profiles flip but also the observed number of arms in
218 cross-polarization is increased, instead of diminished, by an offset of 2 compared to the
219 number of physical grooves. In all datasets, the overall pattern is quite different near the
220 center of the images, i.e., for radiation angles near-normal to the gold film. All co-
221 polarized radiation patterns show a bright feature exactly at $k_{||} = 0$ with a flat phase,
222 while the cross-polarized measurements reveal a donut-shaped feature with a phase
223 advance of $2 \cdot 2\pi$ when traversing a circle around the optical axis. The OAM transfer
224 corresponding to this donut-shaped feature is equal to the change in the SAM ($\Delta\sigma =$
225 ± 2), independent of the geometry or handedness of the grooves. Since this feature
226 persists in the case of a bullseye geometry, we conclude that it arises from light that has
227 undergone spin-to-orbital-angular-momentum conversion caused by the subwavelength
228 aperture and scattered in the normal direction ($k_{||} = 0$) into the far field[44]. This is
229 confirmed at the end of this section by OAM decomposition of the measured fields. In
230 any case, we conclude that the radiation patterns do not map directly onto the well-
231 known OAM-carrying Laguerre-Gauss beams. Instead, the spiral structures scatter into
232 a variety of OAM contributions, the superposition of which is observed as a radiation
233 pattern.

234 The observations indicate that the conversion of input plane waves into output OAM-
235 carrying spherical waves leads to an OAM-mixture, in contrast to the 'binary' selection
236 rules reported earlier[37]. The expected selection rules originate from a simple picture,
237 taking the central aperture as a point launching SPPs that then accumulate propagation
238 delay due to the twist of the spiral grooves, where light is coupled into free space. The
239 resulting superposition of wavefronts at an m-armed spiral results in an offset of m in the
240 OAM index. Spin-to-orbital angular momentum conversion causes an additional offset of
241 ± 2 in the generated OAM mode for helicity-non-conserving detection[41-43]. This leads to
242 the selection rule:

$$\Delta l = m + \Delta\sigma, \quad (2)$$

243 which states that the amount of generated OAM mode difference Δl compared to the
244 input wave (OAM$= 0$ in this work) should be equal to the number of spiral arms m plus
245 the helicity change $\Delta\sigma = 0, \pm 2$ (conserving, resp. conversion from RHC to LHC or vice
246 versa)[37].

247 A main strength of our measurement scheme is that the purity of the selection rule can
248 be quantitatively analyzed by computationally decomposing the complex field into the
249 desired basis. This is done by representing the complex electric field $E(\theta, \phi)$ as a linear
250 combination of OAM states:

$$E(\theta,\phi) = \sum_{l=-\infty}^{\infty} C_l(\theta)\exp(il\phi), \quad (3)$$

251 where, to take into account the spherical nature of the scattered wave, we use spherical
252 coordinates, with coefficients $C_l(\theta)$ defined as

$$C_l(\theta) = \frac{1}{2\pi} \int_0^{2\pi} E(\theta,\phi) \cdot \exp(-il\phi)\, d\phi. \quad (4)$$

253 The complex-valued, azimuthal overlap integral results $C_l(\theta)$ can be used to calculate
254 the polar angle resolved OAM mode density (see Fig. S5 a)-b)). From this, the purity or
255 power of an OAM mode l is derived as

$$p_l = \int_0^{\arcsin(NA)} |C_l(\theta)|^2 \cdot \sin(\theta)\, d\theta. \quad (5)$$

256 Normalizing p_l by the sum of its values results in the modal power spectrum $P_l =$
257 $p_l/\sum_{l=-\infty}^{\infty} p_l$ (see Supplementary for implementation details).

258 As an example, Fig. 5 a) reports the OAM power spectrum for a $m = -5$ spiral in the
259 helicity-non-conserving channel with RHC input, showing dominant contributions at
260 $\Delta l = +2$, $\Delta l = 0$ and $\Delta l = -3$. Fig. 5 b) - d) combines the OAM mode decomposition
261 results for $m = -9$ to $m = 9$ spirals (each OAM power spectrum is normalized to unit
262 integrated content) for three different input-output polarization combinations. Throughout
263 we find dominant features at the selection rule[37], i.e., at the diagonal $l = m$ in the
264 helicity-conserving channels [Fig. 5 b) and Fig. S 5 c)], $l = m \mp 2$ respectively for
265 conversion from LHC to RHC [Fig. 5 c)] and vice versa [Fig. 5 d)]. In addition, we
266 observe strong leakage into the $l = 0$ mode for polarization-conserving measurement,
267 resp. $l = \pm 2$ for the polarization non-conserving data. On average, we identify the
268 purities of the OAM modes following the selection rule to be $(13 \pm 4)\%$ for co-
269 polarization and $(38 \pm 3)\%$ for cross-polarization.

270 In general, the dominant OAM contributions fit the interpretation that only a fraction of
271 the light interacted with the spiral grooves, while the remainder essentially gained no
272 OAM upon direct transmission or gained only OAM corresponding to a change of the
273 SAM, i.e., spin-orbit coupling at the aperture. Additionally, the presence of the OAM
274 mode $l = 0$ in cross-polarization is likely due to the non-perfect extinction ratio of the
275 polarizers employed. While from the perspective of functional nanostructures for
276 generating OAM, it is evident that performance is imperfect, these measurements
277 highlight that our powerful new measurement method allows for an unprecedented

278 quantification. The performance of the nanostructures in terms of OAM mode purity can
279 be further improved by optimizing the geometrical parameters of the spiral such as the
280 aperture radius or by using metal-insulator-metal arrangements[45,46]. Our observation
281 points out that the essential parameter to optimize is the tradeoff between overall
282 transmission efficiency (requires large central aperture) and leakage into OAM$= 0, \pm 2$
283 (requires low direct transmission). Detailed pointers for observation are available in the
284 data as one has the full radiated field at hand. For instance, one can precisely determine
285 the OAM mode density within any given band of angles $\theta, \theta + \Delta \theta$, enabling one to
286 determine the polar angles into which particular OAM content is scattered (see
287 Supplementary).

Method validation and minimum redundancy

289 Returning to our measurement scheme, we note that polarimetry *plus* interferometry
290 provides not only abundant but also redundant information on the wavefront. The reason
291 for this lies in the fact that polarimetry already determines the phase *difference* between
292 orthogonally polarized field components, which should be strictly identical to the
293 difference in phase profiles measured with holography in the same two crossed
294 polarizations. For instance, the following simple combinations of Stokes parameters
295 represent phase difference profiles

$$\arg(S_2 + iS_3) \quad = \varphi_V - \varphi_H \qquad (6a)$$
$$\arg(S_1 - iS_3) \quad = \varphi_A - \varphi_D \qquad (6b)$$
$$\arg(S_1 + iS_2) \quad = \varphi_{LHC} - \varphi_{RHC}, \quad (6c)$$

296 where φ is the phase profile corresponding to the polarization state labeled in the
297 subscript (V=vertical, H=horizontal, A=anti-diagonal, D=diagonal, taken to refer to the
298 camera plane). On one hand, this redundancy can be used to check the *consistency* of
299 the method by comparing maps of phase *differences* determined with polarimetry and
300 holography. On the other hand, one can use the redundancy to reduce the total number
301 of measurements required to fully determine $\mathbf{S}(\theta, \phi)$ (up to an arbitrary phase offset).

302 Figure 6 a) shows an example consistency check through a direct comparison of
303 $\varphi_V - \varphi_H$ and $\arg(S_2 + iS_3)$ again for the case of a $m = -5$ spiral (the remaining two
304 phase difference comparisons listed in Eq. 6 are shown in Fig. S 6). Evidently, these
305 measurements confirm the consistency between phase difference maps obtained using
306 holography and polarimetry, with the only notable distinction lying in the noise
307 characteristics. Stokes polarimetry relies on pixel-by-pixel image subtraction, leading to
308 uncorrelated shot-noise propagating into the phase map. Instead, the holography
309 images are effectively low-pass filtered by the reconstruction procedure (Fourier
310 transform and masking of interferogram).

311 Figure 6 b) provides an example of how the Stokes parameters in combination with a
312 single holography measurement (in this case φ_V) can be used to reconstruct the phase
313 profile in any arbitrary polarization channel. Here, Fig. 6 b) shows the reconstructed
314 phase profile for a $m = -5$ spiral for RHC polarized detection, alongside a direct
315 holographic determination of the phase for comparison. This illustrates how the number
316 of measurements needed to fully quantify a radiation pattern can be reduced. Instead of
317 independent polarimetry and holography measurements for each polarization, it is
318 enough to perform a single holographic measurement plus the four measurements
319 required to retrieve the Stokes parameters (required calculus is described in the
320 Supplementary). In addition, the phase profile reconstructions for four additional
321 polarization channels (vertical, diagonal, anti-diagonal, LHC) are shown in Fig. S 6.
322 These comparisons show excellent agreement.

323 The minimally redundant measurements could be advantageous both from the viewpoint
324 of efficiency as well as reduced requirements on camera dynamic range in polarimetry
325 compared to holographic measurements. Holography works best with a large fringe
326 contrast throughout the recorded interferogram, with fringe intensities spanning the
327 camera dynamic range. This fringe contrast (visibility) increases as the intensity ratio of
328 the two interfering waves (object and reference wave) gets closer to one[31]. For strongly
329 structured radiation patterns, this requirement is difficult to fulfill. The data redundancy
330 enables one to perform the holography just for a polarization channel that has the most
331 suited intensity distribution, i.e., polarization channels where directly transmitted light is
332 (partially) blocked. On top of that, this approach allows for improvements in
333 measurement speed, since the minimum number of required images can be reduced to
334 only four: a single hologram to determine amplitude and phase in one polarization
335 channel, and intensity measurements through three complementary polarizer settings.

Discussion

337 We developed a measurement technique for the characterization of scattered radiation
338 patterns from individual nanoscatters in terms of amplitude, vector, and phase. In
339 principle, the technique could be performed even with a single camera shot, given that
340 off-axis holography requires just a single image and that polarization can be
341 multiplexed[47]. As an example application demonstrating the remarkable insight that this
342 technique can offer for studies of optical antennae, we analyzed the OAM content of
343 light scattered by a family of plasmonic spirals. In contrast, with other OAM
344 measurement techniques, our method does not require the use of spiral phase plates or
345 holograms[23,24], with a single image enabling direct decomposition in OAM contributions.
346 The current limit to our technique is the NA of our microscope objective. Extending the
347 method to a 4π microscopy arrangement could fulfill the quest for full quantification of
348 the multipole content of any scattering geometry using its far field. The presented

349   method will directly apply to many important problems in nanophotonics, such as the use
350   of plasmonic oligomer antennae for sensing and emission, metasurfaces for controlling
351   transmitted and reflected wavefronts that depend on the incident amplitude, phase and
352   vector contents, and nonlinear metasurfaces in which phase gradients imprinted in the
353   metasurface geometry determine the efficiency and angular distribution of, e.g.,
354   frequency conversion. In all these cases, access to angle-resolved amplitude,
355   polarization and phase properties of the far-field is of paramount importance.

Materials and methods

Experimental setup

358   The laser beam (frequency-stabilized Helium Neon laser $\lambda = 633$ nm) is expanded by a
359   telescope ($f = -25$ mm and $f = 200$ mm achromats) and transmitted through the first
360   polarimeter consisting of a linear polarizer LP_1 (Thorlabs LPVIS100) and quarter wave
361   plate QWP_1 (Thorlabs AQWP05M-600), which are used to prepare the incoming
362   polarization state. After LP_1, the beam is split in two by a 50/50 beamsplitter. In the
363   object arm, the beam is weakly focused ($f = 125$ mm) onto the center of a
364   nanostructure. Light scattered by the nanostructure is collected from the patterned gold
365   side by a Nikon LU Plan Apo 100x/0.9 objective. The scattered light is guided through a
366   4f-telescope (two $f_T = 50$ mm lenses), which contains a circular pinhole (diameter of 400
367   μm) as a real space filter to select only the light coming from the nanostructure. The
368   Fourier lens ($f_F = 200$ mm) is placed at a distance $4f_T + f_F$ from the objective back focal
369   plane, just behind the telescope. A second polarimeter consisting of a quarter wave
370   plate QWP_2 (Thorlabs AQWP05M-600) and linear polarizer LP_2 (Thorlabs LPVIS100)
371   projects the outgoing wave onto the desired polarization channel. A half waveplate
372   (Thorlabs AHWP05M-600) is included to rotate the polarization of the object wave back
373   onto that of the reference wave, which is recombined with the object wave using a
374   second 50/50 beamsplitter. The tube lens ($f = 200$ mm) creates a real (Fourier) space
375   image on the CCD (Photometrics CoolSNAP EZ)) in the absence (presence) of the
376   Fourier lens that resides on a flip mount. To increase the dynamic range of our
377   measurement beyond that of the CCD camera, we record the intensity and interference
378   patterns using two different exposure times ($t_1 = 50$ ms and $t_2 = 2000$ ms) and merge
379   the two images by using $I(t_1)$ in a circular region around the high-intensity part of the
380   image and $I(t_2)$ for the remainder, while compensating for the ratio of integration times.
381   The reference beam is attenuated by optical density filters to approximately half of the
382   intensity maximum of the object wave in the co-polarized channel.

Sample design and nanofabrication

384   Samples were fabricated on 170 μm thick glass cover slides with a 5-nm-thick chromium
385   adhesion layer and a 200-nm-thick gold film evaporated on top. Structures were milled

into the gold film using a focused ion beam (FEI Helios). The geometrical parameters are: central aperture diameter $d = 250$ nm, separation of the first groove and the center $a = 375$ nm, width of grooves $w = 250$ nm, pitch of grooves $p = 500$ nm and number of windings $N = 10$. The central aperture is milled entirely through the gold and chromium, while the corrugations are approximately 80 nm deep. While for the bullseye structures, these corrugations are concentric, for the m-armed spirals (m>0 for CW and m<0 for CCW spirals) the radius r depends on the azimuthal angle ϕ according to:

$$r(\phi) = a + m \cdot p \frac{\phi}{2\pi} \quad 0 \le \phi < 2\pi N. \quad (7)$$

In the case of $|m| > 1$, adjacent spiral arms have an angle offset of $\Delta\phi = 2\pi/|m|$. The minimal separation between neighboring spirals is 25 µm to prevent inter-structure coupling.

Stokes and polarization ellipse parameters

The Stokes parameters S_i, where $i = 0,1,2,3$, can be written in terms of orthogonal electric field components E_x and E_y as

$$\begin{pmatrix} S_0 \\ S_1 \\ S_2 \\ S_3 \end{pmatrix} = \begin{pmatrix} \langle|E_x|^2\rangle & + & \langle|E_y|^2\rangle \\ \langle|E_x|^2\rangle & - & \langle|E_y|^2\rangle \\ \langle E_x E_y^*\rangle & + & \langle E_y E_x^*\rangle \\ i(\langle E_x E_y^*\rangle & + & \langle E_y E_x^*\rangle) \end{pmatrix} = \begin{pmatrix} I(0°,0°) & + & I(90°,90°) \\ I(0°,0°) & - & I(90°,90°) \\ I(45°,45°) & - & I(135°,135°) \\ I(0°,45°) & - & I(0°,135°) \end{pmatrix} \quad (8)$$

Here, x and y refer to camera coordinates. We collect the six intensity maps $I(\beta,\gamma)$, i.e., $I_H, I_V, I_D, I_A, I_{RHC}, I_{LHC}$ with the required angles β and γ for QWP_2 and LP_2 indicated in Eq. 8. It should be noted that this set is redundant, as in principle four measurements suffice (e.g., I_H, I_V, I_D, I_{RHC}). The polarization ellipse parameters (sketch shown in Fig. S 2 a)) can be derived from the Stokes parameters using

$$\epsilon = \frac{1}{2} \cdot \arg\left(\sqrt{S_1^2 + S_2^2} + iS_3\right) \quad (9a)$$

$$\alpha = \frac{1}{2} \cdot \arg(S_1 + iS_2). \quad (9b)$$

Phase correction in off-axis holography

In digital holographic microscopy phase aberrations can occur due to the high NA microscope objective and a non-flat phase front for the reference beam[32]. The aberration consists of an overall parabolic phase profile that is present already when imaging a single subwavelength aperture. We perform a numerical correction using the complex conjugate of the spherical phase term that results in the flattest residual when multiplied with the phase measured for a single aperture[32]. This phase correction calibration step needs to be repeated each time the sample position, objective focus or

reference beam tilt angle change. Note, that although the curvature of the parabolic phase correction value does not influence the retrieved OAM power spectrum, lateral misalignments of the phase correction with respect to the propagation axes can cause a minor mode crosstalk.

Simulation procedure

Far-field profile simulations are performed using 3D finite-difference time-domain software (Lumerical FDTD). The bullseye/ spiral structures are modeled using the same parameters as the fabricated structures and are excited using two normally incident plane waves, which are shifted 90° in phase and rotated 90° in polarization (RHC polarized input) and have a wavelength of $\lambda = 633$ nm. The total simulation region has dimensions $(17 \times 17 \times 0.8)\mu m^3$ and is enclosed by perfectly matched layers (PMLs). A mesh grid size of 12 nm is used to model the spiral grooves. The gold film permittivity was modeled using a Drude model fit to values reported by Johnson and Christy[48]:

$$\epsilon_r = \epsilon_\infty - \frac{\omega_p^2}{\omega(\omega + i\gamma)}, \quad (10)$$

where $\epsilon_\infty = 9.54, \omega_p = 1.35 \times 10^{16}$ rad/s and $\gamma = 1.25 \times 10^{14}$ rad/s. The electromagnetic field is recorded using a monitor on a plane located 10 nm above the nanoscatterer; the standard Lumerical Stratton-Chu near to the far-field projection technique is applied to calculate the field 1 m away from the structure. It should be noted that this technique is not rigorous for systems with interfaces.

Acknowledgements

Conflict of interest

The authors declare no conflict of interest.

Contributions

All authors jointly conceived the experimental method. C.H and R.R. realized the set-up, fabricated and designed the samples and performed the measurements. All authors jointly conceived the data analysis method, which was implemented by R.R and C.H.; F. K. supervised the project. R. R., and F. K. wrote the manuscript, which was then revised by all authors.

444 Supplementary information accompanies the manuscript on the Light: Science &
445 Applications website (http://www.nature.com/lsa/)

References

447 [1] Mühlschlegel P, Eisler HJ, Martin OJF, Hecht B, Pohl DW. Resonant optical antennas.
448 *Science* 2005; **308**: 1607-1609.

449 [2] Bharadwaj P, Deutsch B, Novotny L. Optical antennas. *Adv Opt Photonics* 2009; **1**:
450 438-483.

451 [3] Giannini V, Fernández-Domínguez AI, Heck SC, Maier SA. Plasmonic nanoantennas:
452 fundamentals and their use in controlling the radiative properties of nanoemitters. *Chem*
453 *Rev* 2011; **111**: 3888-3912.

454 [4] Lezec HJ, Degiron A, Devaux E, Linke RA, Martin-Moreno L *et al*. Beaming light from a
455 subwavelength aperture. *Science* 2002; **297**: 820-822.

456 [5] Curto AG, Volpe G, Taminiau TH, Kreuzer MP, Quidant R *et al*. Unidirectional emission
457 of a quantum dot coupled to a nanoantenna. *Science* 2010; **329**: 930-933.

458 [6] Dregely D, Taubert R, Dorfmüller J, Vogelgesang R, Kern K *et al*. 3D optical Yagi–Uda
459 nanoantenna array. *Nat Commun* 2011; **2**: 267.

460 [7] Chen YH, Huang L, Gan L, Li ZY. Wavefront shaping of infrared light through a
461 subwavelength hole. *Light Sci Appl* 2012; **1**: e26.

462 [8] Coenen T, Bernal Arango F, Koenderink AF, Polman A. Directional emission from a
463 single plasmonic scatterer. *Nat Commun* 2014; **5**: 3250.

464 [9] Rodríguez-Herrera OG, Lara D, Bliokh KY, Ostrovskaya EA, Dainty C. Optical
465 nanoprobing via spin-orbit interaction of light. *Phys Rev Lett* 2010; **104**: 253601.

466 [10] Kruk SS, Decker M, Staude I, Schlecht S, Greppmair M *et al*. Spin-polarized photon
467 emission by resonant multipolar nanoantennas. *ACS Photonics* 2014; **1**: 1218-1223.

468 [11] Osorio CI, Coenen T, Brenny BJM, Polman A, Koenderink AF. Angle-resolved
469 cathodoluminescence imaging polarimetry. *ACS Photonics* 2016; **3**: 147-154.

470 [12] De Leo E, Cocina A, Tiwari P, Poulikakos LV, Marqués-Gallego P *et al*. Polarization
471 multiplexing of fluorescent emission using multiresonant plasmonic antennas. *ACS Nano*
472 2017; **11**: 12167-12173.

473 [13] Hoang TB, Akselrod GM, Mikkelsen MH. Ultrafast room-temperature single photon
474 emission from quantum dots coupled to plasmonic nanocavities. *Nano Lett* 2015; **16**:
475 270-275.

476 [14] Yu NF, Genevet P, Kats MA, Aieta F, Tetienne JP *et al*. Light propagation with phase
477 discontinuities: generalized laws of reflection and refraction. *Science* 2011; **334**: 333-
478 337.

479 [15] Huang LL, Chen XZ, Mühlenbernd H, Zhang H, Chen SM *et al*. Three-dimensional
480 optical holography using a plasmonic metasurface. *Nat Commun* 2013; **4**: 2808.

481 [16] Karimi E, Schulz SA, De Leon I, Qassim H, Upham J *et al*. Generating optical orbital
482 angular momentum at visible wavelengths using a plasmonic metasurface. *Light Sci*
483 *Appl* 2014; **3**: e167.

484 [17] Huang K, Dong ZG, Mei ST, Zhang L, Liu YJ *et al*. Silicon multi-meta-holograms for
485 the broadband visible light. *Laser Photonics Rev* 2016; **10**: 500-509.

486 [18] Allen L, Beijersbergen MW, Spreeuw RJC, Woerdman JP. Orbital angular momentum
487 of light and the transformation of Laguerre-Gaussian laser modes. *Phys Rev A* 1992; **45**:
488 8185-8189.

489 [19] Wang J, Yang JY, Fazal IM, Ahmed N, Yan Y *et al*. Terabit free-space data
490 transmission employing orbital angular momentum multiplexing. *Nat Photonics* 2012; **6**:
491 488-496.

492 [20] Willner AE, Huang H, Yan Y, Ren Y, Ahmed N *et al*. Optical communications using
493 orbital angular momentum beams. *Adv Opt Photon* 2015; **7**: 66-106.

494 [21] Erhard M, Fickler R, Krenn M, Zeilinger A. Twisted photons: new quantum
495 perspectives in high dimensions. *Light Sci Appl* 2018; **7**: 17146.

496 [22] Padgett M, Bowman R. Tweezers with a twist. *Nat Photonics* 2011; **5**: 343-348.

497 [23] Leach J, Padgett MJ, Barnett SM, Franke-Arnold S, Courtial J. Measuring the orbital
498 angular momentum of a single photon. *Phys Rev Lett* 2002; **88**: 257901.

499 [24] Litvin IA, Dudley A, Roux FS, Forbes A. Azimuthal decomposition with digital
500 holograms. *Opt Express* 2012; **20**: 10996-11004.

501 [25] D'Errico A, D'Amelio R, Piccirillo B, Cardano F, Marrucci L. Measuring the complex
502 orbital angular momentum spectrum and spatial mode decomposition of structured light
503 beams. *Optica* 2017; **4**: 1350-1357.

504 [26] Kulkarni G, Sahu R, Magaña-Loaiza OS, Boyd RW, Jha AK. Single-shot
505 measurement of the orbital-angular-momentum spectrum of light. *Nat Commun* 2017; **8**:
506 1054.

507 27 Whitehouse DJ. *Handbook of Surface and Nanometrology*. 2nd edn. Boca Raton:
508 CRC Press; 2010.

509 28 Lieb MA, Zavislan JM, Novotny L. Single-molecule orientations determined by direct
510 emission pattern imaging. *J Opt Soc Am B* 2004; **21**: 1210-1215.

511 29 Sersic I, Tuambilangana C, Koenderink AF. Fourier microscopy of single plasmonic
512 scatterers. *New J Phys* 2011; **13**: 083019.

513 30 Osorio CI, Mohtashami A, Koenderink AF. K-space polarimetry of bullseye plasmon
514 antennas. *Sci Rep* 2015; **5**: 9966.

515 31 Hariharan P. *Optical Holography*: *Principles*, *Techniques and Applications*.
516 Cambridge: Cambridge University Press; 1996.

517 32 Cuche E, Marquet P, Depeursinge C. Simultaneous amplitude-contrast and
518 quantitative phase-contrast microscopy by numerical reconstruction of Fresnel off-axis
519 holograms. *Appl Opt* 1999; **38**: 6994-7001.

520 33 Suck SY, Collin S, Bardou N, De Wilde Y, Tessier G. Imaging the three-dimensional
521 scattering pattern of plasmonic nanodisk chains by digital heterodyne holography. *Opt*
522 *Lett* 2011; **36**: 849-851.

523 34 Kruk SS, Wong ZJ, Pshenay-Severin E, O'Brien K, Neshev DN *et al*. Magnetic
524 hyperbolic optical metamaterials. *Nat Commun* 2016; **7**: 11329.

525 35 Martinez-Marrades A, Greusard L, De Wilde Y, Bardou N, Collin S *et al*.
526 Characterization of plasmonic nanoantennas by holographic microscopy and scanning
527 near-field microscopy. *Opt Commun* 2016; **359**: 455-159.

528 36 Babocký J, Křížová A, Štrbková L, Kejík L, Ligmajer F *et al*. Quantitative 3D phase
529 imaging of plasmonic metasurfaces. *ACS Photonics* 2017; **4**: 1389-1397.

530 37 Gorodetski Y, Drezet A, Genet C, Ebbesen TW. Generating far-field orbital angular
531 momenta from near-field optical chirality. *Phys Rev Lett* 2013; **110**: 203906.

532 38 Mohtashami A, Osorio CI, Koenderink AF. Angle-resolved polarimetry of antenna-
533 mediated fluorescence. *Phys Rev Appl* 2015; **4**: 054014.

534 39 Garcia-Vidal FJ, Martin-Moreno L, Ebbesen TW, Kuipers L. Light passing through
535 subwavelength apertures. *Rev Mod Phys* 2010; **82**: 729-787.

536 40 Kim H, Park J, Cho SW, Lee SY, Kang M *et al*. Synthesis and dynamic switching of
537 surface plasmon vortices with plasmonic vortex lens. *Nano Lett* 2010; **10**: 529-536.

538 [41] Marrucci L, Manzo C, Paparo D. Optical spin-to-orbital angular momentum conversion
539 in inhomogeneous anisotropic media. *Phys Rev Lett* 2006; **96**: 163905.

540 [42] Bliokh KY, Rodríguez-Fortuño FJ, Nori F, Zayats AV. Spin–orbit interactions of light.
541 *Nat Photonics* 2015; **9**: 796-808.

542 [43] Vuong LT, Adam AJL, Brok JM, Planken PCM, Urbach HP. Electromagnetic spin-orbit
543 interactions via scattering of subwavelength apertures. *Phys Rev Lett* 2010; **104**:
544 083903.

545 [44] Goldstein DH. *Polarized Light*. 3rd edn. Boca Raton: CRC Press; 2010.

546 [45] Zilio P, Parisi G, Garoli D, Carli M, Romanato F. Bilayer holey plasmonic vortex lenses
547 for the far field transmission of pure orbital angular momentum light states. *Opt Lett*
548 2014; **39**: 4899-4902.

549 [46] Garoli D, Zilio P, Gorodetski Y, Tantussi F, De Angelis F. Optical vortex beam
550 generator at nanoscale level. *Sci Rep* 2016; **6**: 29547.

551 [47] Colomb T, Dahlgren P, Beghuin D, Cuche E, Marquet P *et al*. Polarization imaging by
552 use of digital holography. *Appl Opt* 2002; **41**: 27-37.

553 [48] Johnson PB, Christy RW. Optical constants of the noble metals. *Phys Rev B* 1972; **6**:
554 4370-4379.

Figure legends

556 **Figure 1.** Conceptual sketch. A single nanoantenna radiating a spherical wave with a
557 characteristic phase profile as well as amplitude and polarization. This spherical wave is
558 transformed into a plane wave in the back focal plane of a microscope objective.
559 Measuring the amplitude, polarization and phase content of the light over all angles
560 enables detailed reconstruction of the antenna physics.

561 **Figure 2.** Schematic view of the setup and plasmonic spiral antenna. (**a**) Combined
562 Fourier polarimetry and holography setup, consisting of a transmission microscope, two
563 polarimeters and a reference beam. The microscope contains a 4f-telescope for spatial
564 filtering of light from a single antenna. (**b**) Principle of plasmonic bullseye/spiral
565 nanostructure. Light impinging from the glass side excites the single hole in a thick metal
566 film. SPPs launched by the hole at the air side scatter out at the spiral corrugation. The
567 red arrows denote the directions of the SPP and free-space electric fields. (**c**) SEM
568 micrograph of a $m = -5$ spiral antenna.

569 **Figure 3.** Demonstrations of Fourier microscopy, polarimetry and holography. (**a**)
570 Fourier map of intensity, (**b**) polarization ellipse parameters ϵ and α, (**c**) Digital Fourier

571 transform of an interferogram obtained with RHC polarized detection, (**d**) reconstructed
572 phase profiles for RHC and LHC polarized detection. In all sub-figures, RHC polarized
573 input and a $m = -5$ spiral nanostructure were used. The green and red arrows indicate
574 the input and output polarizations, respectively.

575 **Figure 4.** Measured (**a** and **c**) and simulated (**b** and **d**) combined amplitude and phase
576 profiles for $m \leq 0$ nanostructures. Field profiles in the Fourier plane of a bullseye ($m =$
577 0) and $m = -3, -6, -9$ spirals. The transmitted polarization channels are co- (**a-b**) and
578 cross-polarized (**c-d**) with RHC polarized input. The plots show a combined
579 representation for the phase as hue and field amplitude as brightness (logarithmic
580 scale). The green and red arrows indicate the input and output polarizations,
581 respectively. Each amplitude profile is normalized by its maximum. A circular
582 representation of the color map used here is given in Fig. S3 c).

583 **Figure 5.** OAM decomposition results. (**a**) OAM power spectrum for a $m = -5$ spiral with
584 RHC input and LHC output. (**b-d**) OAM power spectra as a function of m in co- (**b**) and
585 cross-polarization (**c** and **d**) with RHC (**b** and **d**) and LHC (**c**) polarized input. The
586 dashed lines in (**b-d**) indicate $l = m$. Sub-figures (**c**) and (**d**) have the same color scale.

587 **Figure 6.** Validation and redundancy removal in combined holographic and polarimetric
588 measurements. (**a**) Difference between phase profiles with vertical and horizontal output
589 polarizations retrieved using polarimetry and holography. (**b**) Example of a phase profile
590 with RHC polarized output, which was retrieved using a combination of polarimetry and
591 holography, with the correspondent purely holographic profile shown for comparison. In
592 both cases a RHC polarized input and a $m = -5$ spiral were used. The green and red
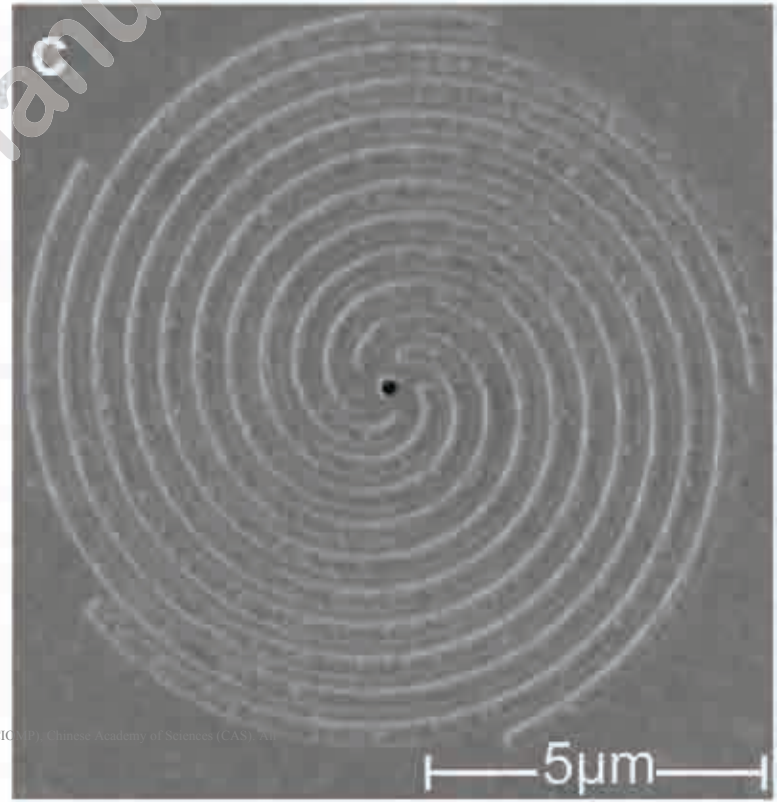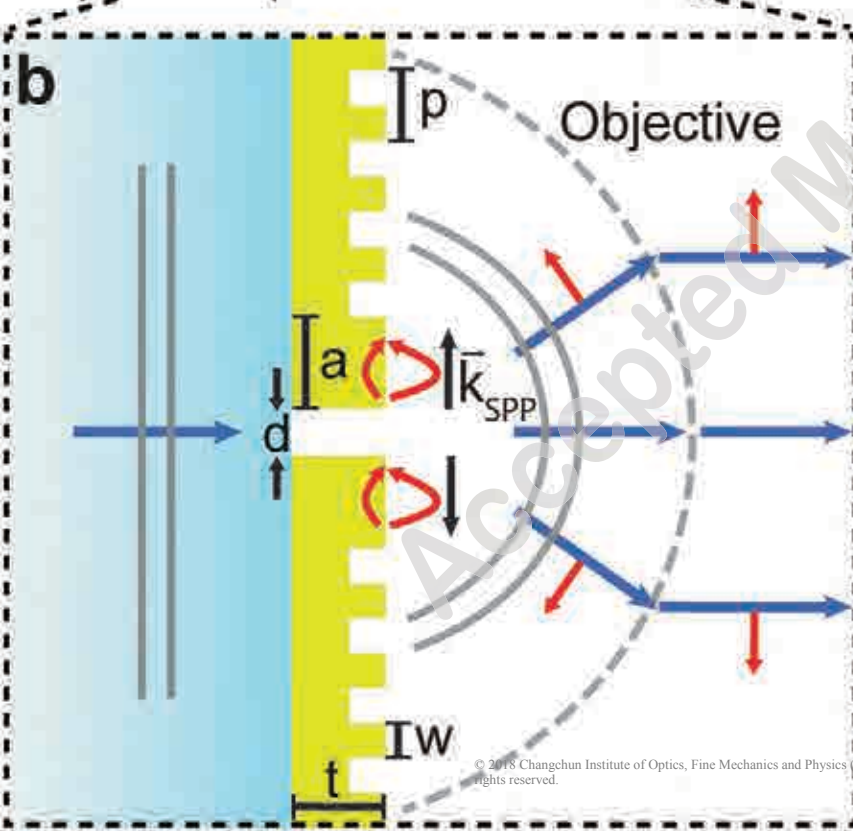593 arrows indicate respectively the input and output polarizations.

$$\mathbf{S}(\theta,\phi)\frac{e^{ikR}}{R}$$

$$\mathbf{S}(\theta,\phi)$$
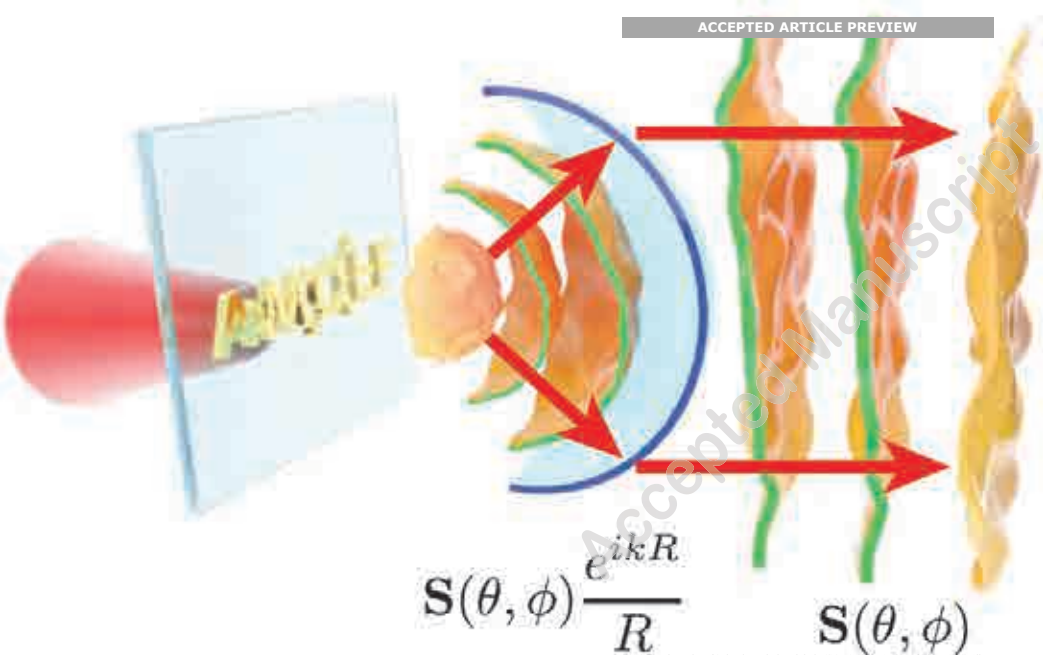
Fourier microscopy
$|\mathbf{S}(k_x,k_y)|^2$

+

Fourier polarimetry
S_0, S_1, S_2, S_3

+

Off-axis holography
$\varphi(k_x,k_y)$

a

LP$_1$ QWP$_1$ Sample 4f-telescope QWP$_2$ LP$_2$ HWP

Fourier lens

CCD

b

p

Objective

a

$\bar{k}_{SPP}$

d

w

t

c

5μm

Fourier microscopy
$|\mathbf{S}(k_x, k_y)|$

a Intensity (counts)

$10^0 \quad 10^1 \quad 10^2 \quad 10^3$

Fourier polarimetry
S_0, S_1, S_2, S_3

b Ellipticity angle (rad)

$-\pi/4 \quad 0 \quad \pi/4$

Ellipse orientation (rad)

$-\pi/2 \quad 0 \quad \pi/2$

Off-axis holography
$\varphi(k_x, k_y)$

c $\mathcal{F}\{H_{RHC}\}$

$10^{-6} \quad 10^{-4} \quad 10^{-2} \quad 10^0$

d Phase (rad)

$-\pi \quad 0 \quad \pi$

a

$\arg(S_x + iS_y)$

[Polarimetry]

$\varphi_\_ - \varphi_\_$

[Holography]

b

Combination of polarimetry & holography:

$$\{ S_0, S_1, S_2, S_3 \} \& \varphi_V \rightarrow \{ \varphi_{LHC}, \varphi_{RHC}, \varphi_H, \varphi_D, \varphi_A \}$$

φ_{RHC}

[Polarimetry & holography]

φ_{RHC}

[Holography]